Atmospheric Environment 129 (2016) 43–54

Contents lists available at ScienceDirect

Atmospheric Environment

journal homepage: www.elsevier.com/locate/atmosenv

Dust-induced radiative feedbacks in north China: A dust storm episode modeling study using WRF-Chem

Lixia Liu [a, b], Xin Huang [a, b, *], Aijun Ding [a, b, **], Congbin Fu [a, b]

[a] Institute for Climate and Global Change Research & School of Atmospheric Sciences, Nanjing University, Nanjing, 210023, China
[b] Collaborative Innovation Center of Climate Change, Jiangsu Province, China

HIGHLIGHTS

- Radiative behaviors of dust differ in source regions and downwind areas.
- Dust stabilizes daytime PBL whereas it poses an opposite effect at night.
- Enhanced nighttime convection promoted the long-range transport of dust.

ARTICLE INFO

Article history:
Received 30 September 2015
Received in revised form
7 January 2016
Accepted 9 January 2016
Available online 11 January 2016

Keywords:
Asian dust
Radiative effects
Boundary-layer meteorology
Feedback
WRF-Chem

ABSTRACT

Radiative forcing of dust aerosol and the radiative feedbacks on the planetary boundary layer (PBL) in North China during a typical Asian dust storm in the early April of 2011 was investigated by an online coupled meteorology-chemistry-aerosol model WRF-Chem. Dust-induced daily mean radiative forcing (RF) at the ground surface and in the atmosphere were estimated to be −21.1 W m^{-2} and 12.7 W m^{-2}, respectively, over Gobi desert, and −13.1 W m^{-2} and 4.8 W m^{-2}, respectively, in downwind region over the North China Plain (NCP). Comparatively, radiative perturbation on short-wave radiation was approximately twice that on long-wave radiation in magnitude. In the daytime, when solar radiation dominated, the surface cooling and atmospheric heating due to dust increased PBL stability, leading to reductions of PBL height (PBLH) about 90 m and decreases in wind speed up to 0.4 m s^{-1}. On the contrary, the radiative forcing in terrestrial radiation caused an opposite response at night, especially in the downwind region. Although dust emission was repressed by weakened wind speed during daytime, the elevated PBLH along with larger deflation at night lifted more dust particles to higher altitude (by up to 75 m in average), which prolonged dust residence time in the atmosphere and further intensified dust loading in downwind areas. Taking dust radiative feedbacks into consideration notably narrowed gaps between model-predicted air temperature vertical profiles with corresponding observations, suggesting a significant importance of dust-radiation interaction in PBL meteorology during dust storms.

1. Introduction

Aerosol-radiation interaction and the feedbacks between meteorological processes and aerosol cycle have caused widespread concerns recently and have been proven to be significant in climate change, weather and air quality (Forkel et al., 2012; Ding et al., 2013; IPCC, 2013; Wang et al., 2014). As a main contributor to the global aerosol burden, mineral dust exerts more complex perturbations in radiation transfer than purely scattering aerosols through scattering, absorbing solar radiation and emitting terrestrial radiation (Alpert et al., 1998), making it particularly pronounced in aerosol-radiation interaction investigations.

Eastern Asia is one of the world's largest dust source regions, with about 800 Tg mineral dust emitted annually into the atmosphere (Zhang et al., 1997), accounting for up to 10–25% global dust load (Tegen and Schepanski, 2009). Dust storms, which mostly occur in spring associated with active cold fronts, typically originate from desert regions in northwest and north of China, such as Taklimakan and Gobi Deserts (Alizadeh Choobari et al., 2014), and spread southeastward over the East Asian Continent, even across

* Corresponding author. Institute for Climate and Global Change Research & School of Atmospheric Sciences, Nanjing University, Nanjing, 210023, China.
** Corresponding author. Institute for Climate and Global Change Research & School of Atmospheric Sciences, Nanjing University, Nanjing, 210023, China.
E-mail addresses: xinhuang@nju.edu.cn (X. Huang), dingaj@nju.edu.cn (A. Ding).

http://dx.doi.org/10.1016/j.atmosenv.2016.01.019
1352-2310/

the Pacific Ocean (Husar et al., 2001; In and Park, 2002), causing propagated climatic and environmental influence along the pathways (Park et al., 2005; Nie et al., 2014; Xie et al., 2015). The North China Plain, as a mainly region along the main track of Asian Dust storm, is severely affected by frequent dust events in springtime (Zhang, 2003, 2005; Yuan et al., 2008). Furthermore, existing observations have identified that Asian dust tends to be more absorbing, with single-scattering albedo (SSA) value as low as 0.76 at 500 nm, much smaller than the corresponding values measured in Africa (Costa et al., 2006). Such tremendous dust emissions together with a relatively high absorbing efficiency could pose significant perturbations in Earth's radiative budget in the northern part of China, which has been extensively proved by in-situ measurements, satellite retrievals as well as numerical simulations (Park et al., 2005; Huang et al., 2009; Ge et al., 2010; Kuhlmann and Quaas, 2010; Liu et al., 2011; Chen et al., 2013; Huang et al., 2015).

The short-wave RF due to an Asian dust storm was estimated to be -5.5 W m^{-2} and -9.3 W m^{-2} at the top of the atmosphere (TOA) and at the surface, respectively, based on a coupled regional atmosphere (RAMS)/chemistry (Chemical Weather Forecast System, CFORS) model (Seinfeld et al., 2004). By using RegCM3/dust model, Zhang et al. (2009) conducted a 10-year simulation, and reported a seasonally mean net RF of -5 W m^{-2} and -15 W m^{-2} at TOA and surface over East Asia. Han et al. (2012) pointed out that the short-wave and long-wave RF due to dust at the surface were -90 W m^{-2} and 40 W m^{-2} for dust source region in East Asia, highlighting the climatic importance of dust-induced long-wave radiation. Given the important role of dust in long-wave radiation transfer (Brindley and Russell, 2009; Yue et al., 2010; Wang et al., 2013), some previous studies (i.e. Seinfeld et al., 2004; Ahn et al., 2007; Wang et al., 2010), which did not include dust's perturbation on long-wave radiation transfer, might lead to considerable biases in radiative budget estimation. In addition, the “off-line” method used in previous studies only calculated one-way instantaneous RF (Ahn et al., 2007), failing to represent the radiative effect associated with adjustments in both dust and meteorological fields. The effects of dust RF for both long-wave and short-wave radiation on meteorology, especially on PBL evolution, have not been fully explored yet. Besides, since dust emission and the further long-range transport are highly meteorology-dependent, how the dust-induced radioative perturbations affect its own emission intensity and long-range impact needs further investigations.

Here, we made a short-term regional simulation by using a fully chemistry-meteorology coupled model WRF-Chem. (the Weather Research and Forecasting model coupled with Chemistry) to comprehensively assess the radioative perturbations caused by Asian dust and the subsequent interactions with PBL evolution for both dust source regions and downwind areas. Additionally, the mutual influences between dust emission and meteorology triggered by dust storms were also discussed in detail. This paper is structured as follows: in Section 2 we describe the adopted observation datasets, numerical model and our experiment design; in Section 3 we represent main results which include evaluating the model results with observation in Section 3.1, quantifying dust direct RF and energy budget perturbation in 3.2, discussing the response of PBL meteorology, dust emission and transport in section 3.3 and 3.4, respectively.

2. Methodology and data

2.1. Numerical simulations

WRF-Chem is a three-dimensional Eulerian chemical transport model that considers the complex physical and chemical processes (i.e. emission and deposition, advection and diffusion, aerosol dynamics, etc.), and it fully integrates meteorology and chemistry with aerosol-radiation-cloud feedback processes (Grell et al., 2005). The WRF-Chem version 3.6 was used here to investigate dust radiative feedbacks during the dust storm in the early April of 2011. A model domain with 164 × 86 grids and a horizontal resolution of 20 km was employed, which covered the entire North China including Gobi desert, the major source of the dust episode in this study (see Fig. 1). Thirty vertical layers extended from the ground to 50 hPa were used, with much denser in the lower atmosphere for the purpose of better resolving PBL processes. The initial and boundary meteorological conditions were derived from the 6-h National Centers for Environmental Prediction (NCEP) Final Analysis (FNL) data with 1 × 1° spatial resolution. The simulation period was from 26 March 2011 to 8 April 2011, with the first 10-day simulation as spin-up.

Previous investigations and sensitivity tests indicated that the options of PBL and Land-surface schemes significantly influence the calculation of aerosol-radiation feedback (Alizadeh Choobari et al., 2012), for which determined moisture content in soil, exchange of atmosphere-land and transport processes in the lower atmosphere. Here we adopted the YSU PBL scheme which calculated non-local turbulent fluxes in large-scale eddies, combined with the Noah land-surface scheme and the Monin-Obukhov surface layer scheme as suggested (Alizadeh Choobari et al., 2012). Detailed configurations are listed in Table 1.

To describe dust emissions, GOCART dust emission module (Ginoux et al., 2001) was used in this study, which calculated the dust emission flux F as follows:

$$F = CSs_p u_{10m}^2 (u_{10m} - u_t)(u_{10m} \geq u_t),$$

where C is an empirically derived constant equal to 1 μg s^2 m^{-5}; S denotes the source function based on soil erodibility by wind (shown in Fig. 1); s_p represents the fraction of each size class in erodible dust, including clay, silt and sand which are in different particle size range; u_{10m} is the horizontal wind speed at 10 m altitude which comes from the meteorological output; while u_t is the threshold velocity depending on particle size and soil moisture.

MOSAIC (Model for Simulating Aerosol Interactions and Chemistry) aerosol scheme based on a sectional approach was selected in this simulation (Zaveri and Peters, 1999, 2008). The size distribution of dust was divided into four discrete size bins defined by their lower and upper dry particle diameters (0.039–0.156, 0.156–0.625, 0.625–2.5, and 2.5–10.0 μm). In each size bin, particles were assumed to be spherical. The refractive index of dust has always been a controversial issue, which depends on the composition and wavelengths. A typical value has been assumed as *1.53 + 0.006i* based on several models (Dey, 2004). During the dust events in Beijing from 2004 to 2006, real and imaginary parts of the dust refractive index at 440–1020 nm ranged from 1.52 to 1.56, 0.007 to 0.010, respectively (Wu et al., 2009). Measurements on mineral dust absorptive properties at Lanzhou (dust source region) indicated that the imaginary part of dust was around 0.005 during springtime (Logan et al., 2013). Nakajima et al. (1989) and Fukushima et al. (2000) suggested the imaginary part of Asian dust to be 0.005 and 0.006, respectively. An averaged imaginary part of 0.007 for solar spectrum was recommended for Gobi desert dust (Stone et al., 2007). According to these recommended value and field observations, we assumed that the short-wave refractive index of *1.55 + 0.006i* was acceptable as the refractive index of Asian dust for this case study. The long-wave refractive index of dust was strongly wavelength-dependent, and we adopt the recommended values from the Optical Properties of Aerosols and Clouds dataset (Hess et al., 1998; Zhao et al., 2010). Based on refractive index and

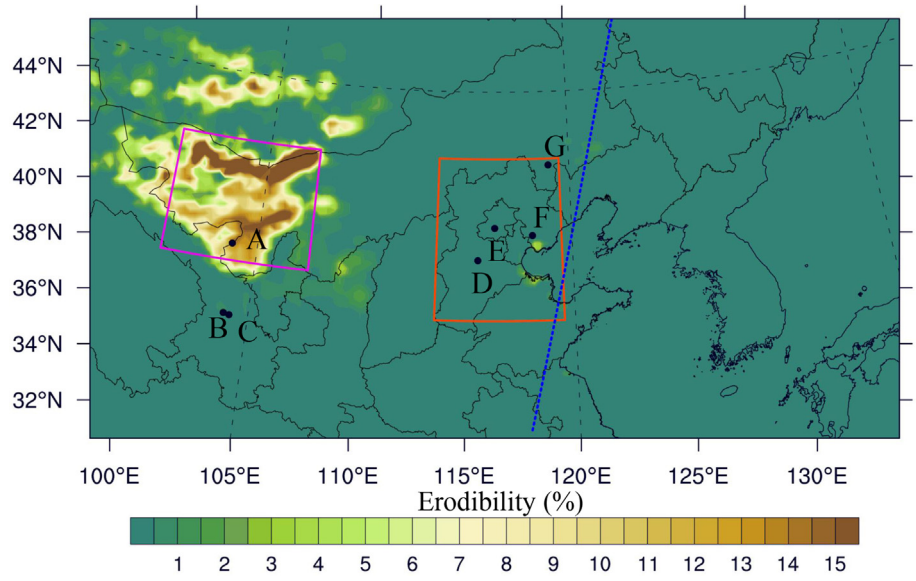

Fig. 1. Model domain with the indication of soil erodibility (%). Squares represent the dust source region (magenta) and the North China Plain (orange). Dots A-G represent Minqin, Lanzhou, Yuzhong, Baoding, Beijing, Tangshan and Chifeng, respectively. The blue line marks the track of CALIPSO satellite on 18:03 UTC 8 April 2011, and the vertical cross-section of which is plotted in Fig. 12. (For interpretation of the references to colour in this figure legend, the reader is referred to the web version of this article.)

Table 1
WRF-Chem configuration options for physical and chemical parameterizations.

Physical and chemical process	configuration
Microphysics	Single-Moment 5-class
Long-wave radiation	RRTMG
Short-wave radiation	RRTMG
Surface layer	Monin-Obukhov
Land-surface model	Noah
Boundary layer scheme	YSU
Cumulus parameterization	Grell 3D
Dust emission estimation	GOCART
Aerosol scheme	MOSAIC

size distribution, optical properties of mineral dust, including extinction coefficient, single-scattering albedo and asymmetry factor, were calculated according to Mie-algorithm, for each size bin and wavelength (4 wavelengths for short-wave radiation 16 wavelengths for long-wave radiation) (Fast et al., 2006). Angstrom exponent was used to convert optical properties to wavelengths needed by radiation schemes and then dust optical properties and radiative feedback could be coupled with the radiative transfer model RRTMG for both short- and long-wave radiation (Zhao et al., 2011).

We performed two parallel simulations, the control experiment (CTL) and the other one with dust's radiative feedbacks (RFB), to investigate dust-radiation feedback and following perturbations in PBL meteorology. Domain settings and model configurations for these two simulations were exactly the same as described before except for the consideration of dust-radiation feedback. That is, the optical properties were taken into account in the calculation of RRTMG radiation transfer in RFB simulation. By contrary, in the CTL simulation, neither long-wave radiation nor short-wave radiation were affected by mineral dust. The differences between these two parallel simulations were considered as dust-induced radiative effects.

2.2. Data

In order to validate model's performance on the reproduction of meteorology and particle pollution, several relevant observations were used in this study. We collected ground-based hourly meteorological data from the Integrated Surface Hourly (ISH) Data archived at the National Climatic Data Center (NCDC) at several monitoring stations: Minqin (103.1 °E, 38.6 °N), Lanzhou (103.9 °E, 36.1 °N), Baoding (115.5 °E, 38.7 °N), Tangshan (118.1 °E, 39.7 °N) and Beijing (116.6 °E, 40.1 °N). In the meantime, available radiosonde observations from the Integrated Global Radiosonde Archive (IGRA) for another two sites Yuzhong (104.1 °E, 35.8 °N) and Chifeng (118.8 °E, 42.3 °N) were utilized to testify the vertical profile of meteorological parameters. The IGRA sounding observation was conducted at 08:00 and 20:00 local time (LT). Note that throughout this paper the time referred to LT, unless UTC was specially mentioned. Daily Air Pollution Index (API), which was acquired through the online access to ambient air monitoring data publicly released by the Ministry of Environmental Protection, was used to deduce daily mean PM_{10} concentrations and compared with the corresponding simulations. The Aerosol Robotic Network (AERONET) has ~100 identical, globally distributed sun- and sky-scanning ground-based automated radiometers, which provides measurements of aerosol optical properties throughout the world (Holben et al., 2001). The available AOD (Aerosol Optical Depth) measurements at Beijing and Lanzhou during April 2011 were introduced for the comparison with modeled hourly AOD. We selected the Level 2.0 AOD data and Level 1.5 size distribution and SSA inversion products at these two sites, which give more quality-controlled information. Simultaneously, satellite-retrieved 550-nm AOD from MODIS (MODerate resolution Imaging Spectroradiometer, MYD08) was also included in this study. In addition, the CALIPSO Level 2 aerosol profile and vertical feature mask datasets were used to provide information of vertical distribution and transport of dust aerosols (Liu et al., 2013).

3. Results and discussions

3.1. Dust episode and model evaluation

The dust episode, which was companied by cold air passage, swept over China from 5 April to 8 April, 2011. As shown in Fig. 2a, The Mongolian cyclonic depression over Gobi desert along with the

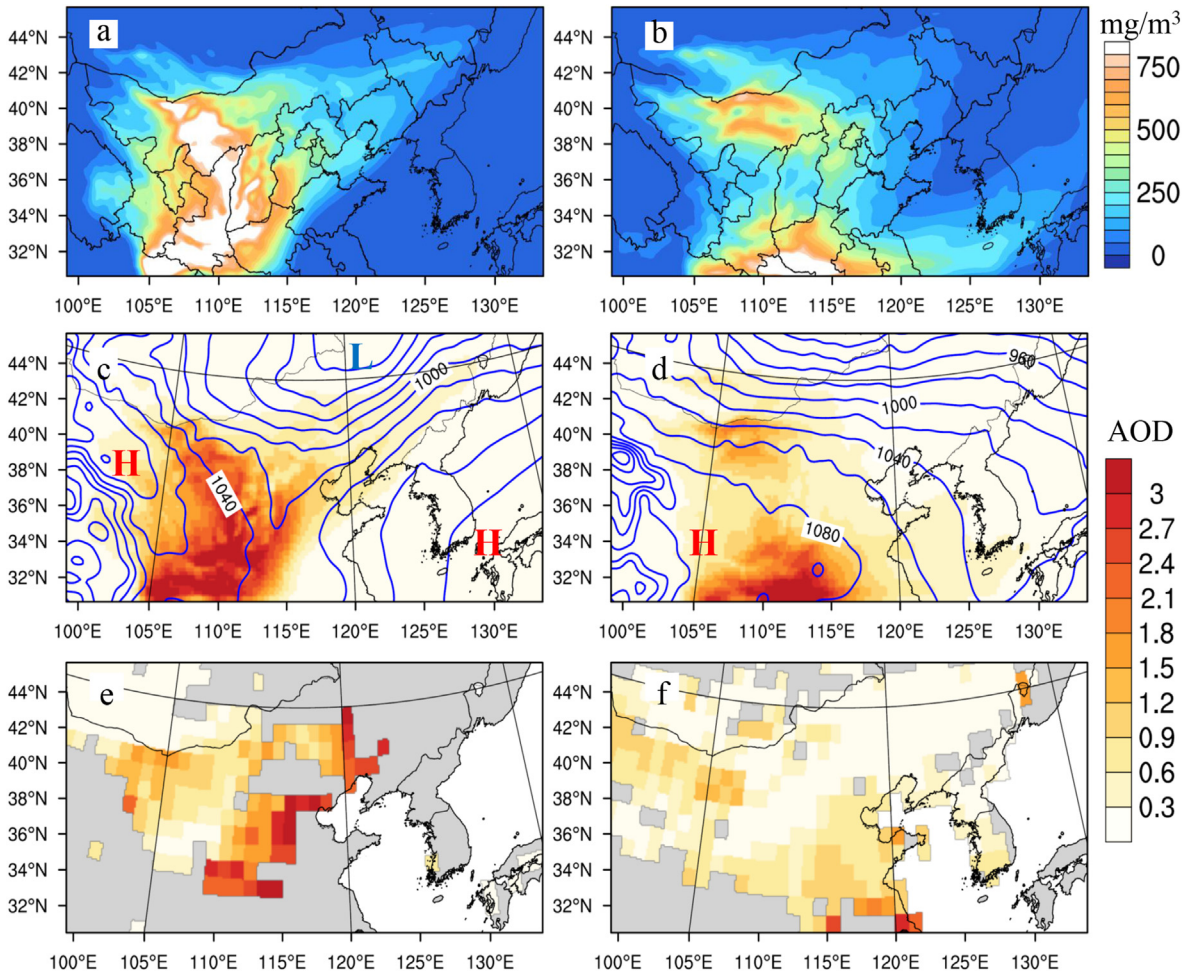

Fig. 2. Spatial patterns of modeled dust column concentration from CTL (a, b), modeled AOD from CTL (c, d), and the corresponding MODIS retrievals (e, f). Blue lines show the 850 hPa geopotential height from NCEP/FNL reanalysis data. Column 1 is for daily mean of 6 April and column 2 is for 8 April. (For interpretation of the references to colour in this figure legend, the reader is referred to the web version of this article.)

followed Siberian high-pressure led to strong northwest wind manifested by intensified isobars, which promoted dust deflation efficiency. The high wind speed and ascendant air flow associated with Mongolian cyclone pushed large load of dust into the downwind area. On 6 April, high AOD value exceeding 1.5 (500 nm) was captured by MODIS over the Gobi desert and a belt stretching towards Northeast China along the west edge of the NCP (Fig. 2c). The simultaneous AERONET AOD value reached up to 1.2 at Beijing (Fig. 3c). These characteristics were generally reproduced by our model simulation. A maximum PM_{10} of approximately 500 μg m^{-3} and 400 μg m^{-3} appeared on the morning of 6 April and 7 April, at Lanzhou and Beijing, respectively (Fig. 3a, b), and the day-to-day variation pattern was similar with observations at these two sites. By 8 April (Fig. 2b), cyclonic depression moved eastward to the North Pacific, leaving the continent under the control of high-pressure subsiding system. Observed AOD in the domain almost decreased to lower than 1.0 (500 nm), and PM_{10} in Beijing dropped down to 90 μg m^{-3} (Fig. 3a), marking the end of this dust storm. Model results showed good agreement with horizontal distribution of MODIS AOD and temporal evolution of AERONET AOD and surface PM_{10}. Generally, an underestimation was made by simulation, which was especially prominent at the NCP area with quite amount of anthropogenic aerosols and during period before/after dust episode when dust wasn't predominant aerosol component. It was expected because that PM_{10} and AOD from observation contained all aerosol species with dynamic diameter less than 10 μm while our model only take mineral dust into account. As important factors in aerosol radiative effect, aerosol size distribution was basically consistent between results from simulation and AERONET INVERSION in pattern and magnitude (Fig. 3e, f), and modeled SSA (600 nm) of 0.919 and 0.961 was comparable to observation of 0.908 and 0.956 in Beijing and Lanzhou, respectively.

To give a quantified evaluation of the model performance in meteorology prediction, we compared modeled 2-m temperature (T2) of the two parallel simulations with corresponding ground-based observation at 5 stations (Minqin, Lanzhou, Baoding, Tangshan and Beijing, the locations are shown in Fig. 1). The evaluation from 5 to 8 April was divided into daytime and nighttime (0800–2000 LT was regarded as daytime here). The statistical indexes like mean bias error (MBE), root mean square error (RMSE) and correlation coefficient (R) were presented in Table 2. It can be seen that the CTL modeling was overall skilled in reproducing the magnitude and temporal variation of T2, with an overall MBE and R of 0.30 and 0.93, respectively. However, it tended to overestimate daytime surface temperatures but under-predict those during nighttime. By contrast, considering dust radiative perturbations, namely RFB, substantially narrow these gaps and thus improved the model performances on T2 prediction. The cooling deviation during daytime and a warming bias at night in RFB was the main issue to be further addressed in the following discussions.

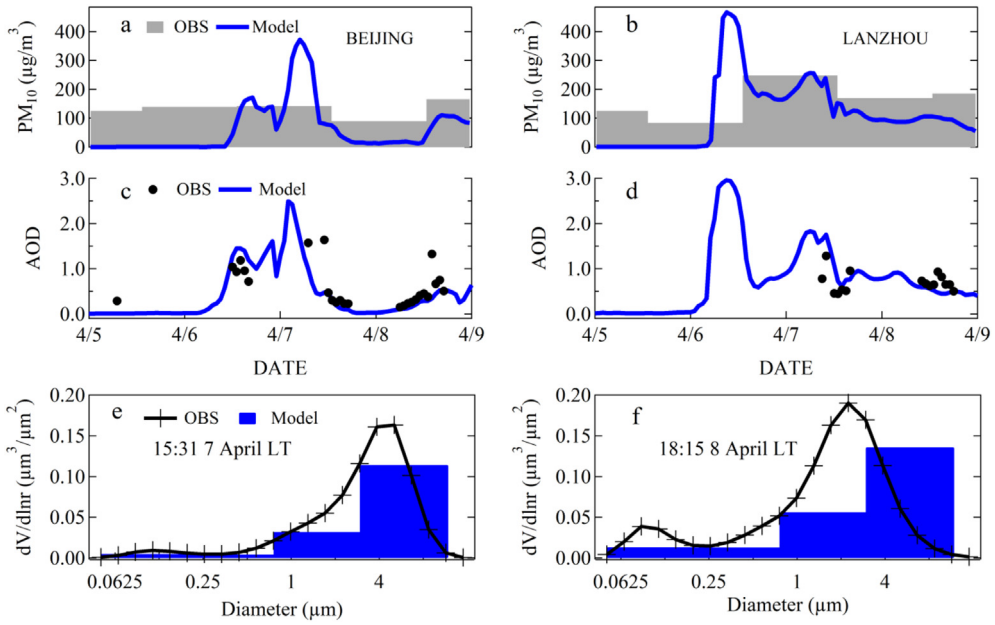

Fig. 3. Comparison of modeled surface PM_{10} concentrations from CTL simulation with the corresponding observations derived from API index at Beijing (a) and Lanzhou (b); AOD at 500 nm of simulation with AERONET observations (c, d); and size distribution of simulation with AERONET INVERSIONS (e, f).

Table 2
Statistical analyses of the simulated daytime and nighttime hourly 2-m temperature versus the ground observations during 5–8 April, 2011.

	CTL			RFB		
	Daytime	Nighttime	All	Daytime	Nighttime	All
MBE[a]	1.02	−0.53	0.30	0.67	−0.51	0.12
RMSE[a]	5.90	4.12	5.02	4.24	3.88	4.03
R[a]	0.93	0.90	0.93	0.94	0.91	0.94

[a] MBE, RMSE and R refer to mean bias error, root mean square error and correlation coefficient, respectively.

3.2. Effects on radiation and energy balance

Fig. 4a and c shows daily mean short-wave RF averaged from 5 to 8 April at the surface and in the atmosphere. Although cloud fraction could be influenced by semi-direct effect of dust (Huang et al., 2006), there was no cloud cover change between CTL and RFB due to little cloud over both the source region and the downstream NCP during the episode according to the satellite observations. Therefore, simulated RF was totally induced by dust-radiation interaction. Incident short-wave radiation arriving at the surface was weakened because that dust scattered and absorbed solar radiation; while in the atmosphere more energy was trapped as dust absorbed solar radiation efficiently. The domain averaged surface and atmospheric solar RF values were −34.6 W m^{-2}, 24.6 W m^{-2} at the source region and −20.3 W m^{-2}, 10.7 W m^{-2} at the NCP, which were close to estimates based on observation (Ge et al., 2010). Conversely, the increased downward long-wave energy reaching the ground by the dust layer led to a positive infrared RF at the surface and a deficit in the radiative budget in the atmosphere. The simulated RF of 13.5 W m^{-2} (source) and 7.2 W m^{-2} (NCP) at the surface in the present work are similar to the WRF-Chem simulation over West Africa (Zhao et al., 2011). Dust exerted comparable magnitude infrared RF as that of solar radiation because coarse particles interfere strongly with long-wave radiation according to Mie theory, which would inevitably cause notable impacts especially at night (Stier et al., 2007).

The surface radiative forcing gave rise to substantial adjustments in sensible and latent heat, as seen in Table 3. In daytime, the decrease in solar radiation reaching ground overtook the increase in infrared radiation, and resulted in negative surface net RF in both the NCP (−24.1 W m^{-2}) and the source region (−52.5 W m^{-2}). It was responsible for the reduction in sensible and latent heat which indicated less thermal and vapor transfer from surface to atmosphere, and could further influence air temperature and precipitation (Miller, 2004). During nighttime, perturbation of long-wave radiation existed alone, and contrast effects were generated in a moderate magnitude. The adjustment in latent heat was not as evident as sensible heat, especially at the source region, which was mostly covered by desert with little moisture, as latent flux was regulated by surface-air humidity exchange.

RF in the overall atmosphere column was interpreted by radiative heating rate which was calculated from radiation fluxes gradient. Daytime and nighttime averaged atmospheric heating rate due to short-wave and long-wave radiation as well as the dust concentration profiles are shown in Fig. 5. Since soil-derived dust usually transports at a high altitude (i.e. typically in upper PBL) (Chun et al., 2001), dust concentration peaked at about 2 km at the downstream NCP while decreased with height throughout the atmosphere at the source region, which was substantially similar during day and night. Dependent on the dust profile, solar irradiance was absorbed by dust particles and transferred to heat, with largest heating rate at about 2 km at the NCP while near the ground surface at the source region. As the absorbed radiation (including both long-wave and short-wave) was re-emitted by suspended dust as infrared radiation, a substantial long-wave radiative cooling was caused by the dust layer. In daytime, as heat was conducted from ground to upper air, dust aerosol was in higher temperature and emitted more infrared near surface, which led to a maximum of long-wave cooling rate occurring near surface. Overall, the short-wave heating dominated in the upper air while long-wave cooling prevailed at lower level, with a value of about 1 K dy^{-1} and −4 K dy^{-1} in source region, which were one order of magnitude larger than those in Australia (Alizadeh Choobari et al., 2014). During nighttime, the surface heat flux was very weak and the

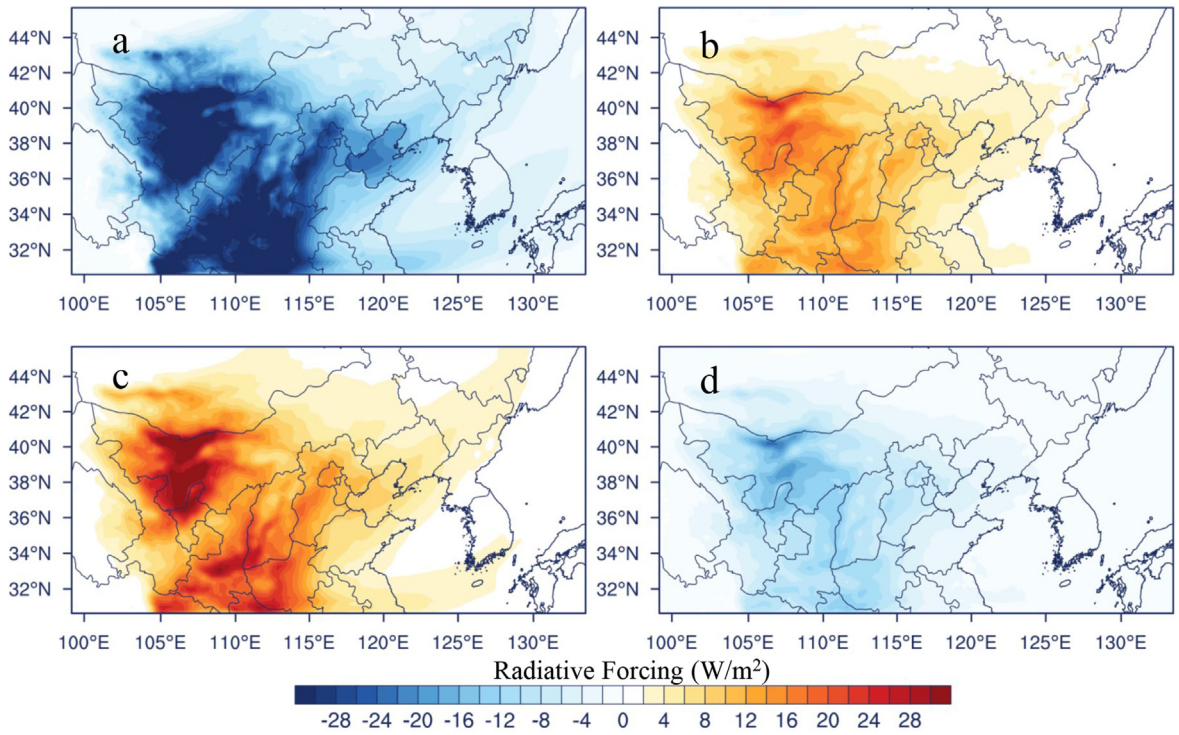

Fig. 4. Spatial distributions of daily mean RF at the surface (a–b) and in the atmosphere (c–d) for short-wave (left panel) and long-wave radiation (right panel) during 5–8 April, 2011.

Table 3
Averaged differences between RFB and CTL during 5–8 April, 2011.

		NCP		Source region	
		Daytime	Nighttime	Daytime	Nighttime
Perturbations in energy budget	short-wave RF at SUF (W m^{-2})	−20.3		−34.6	
	short-wave RF in ATM(W m^{-2})	10.7		24.6	
	long-wave RF at SUF (W m^{-2})	7.2		13.5	
	long-wave RF in ATM(W m^{-2})	−5.9		−11.9	
	sensible heat(W m^{-2})	−13.0	0.9	−29.8	1.3
	latent heat(W m^{-2})	−2.2	0.1	−1.5	0.1
PBL response	2 m temperature (°C)	−0.27 (2.4%)	0.21 (3.5%)	−0.34 (4.9%)	0.17 (1.2%)
	2 m relative humidity (%)	0.72	−0.35	0.43	−0.03
	10 m wind speed (m s^{-1})	−0.3 (3.4%)	0.1 (5.2%)	−0.4 (3.1%)	0.2 (4.5%)
	PBLH (m)	−83.6 (8.0%)	34.4 (10.6%)	−90.2 (9.3%)	75.3 (12.7%)
Dust cycle	emission (mg m^{-2} dy^{-1})			−11.7 (13.5%)	0.2 (2.6%)
	column loading (mg m^{-2})	8.7 (2.1%)	2.1 (0.4%)	−8.0 (0.6%)	−26.2 (3.1%)

[a]SUR and ATM mean the ground surface and the atmosphere, respectively.

long-wave cooling rate relied more on dust vertical distribution. The maximum cooling of −0.3 K dy^{-1} and −1.5 K dy^{-1} was found at 2 km and near surface in the NCP and source regions, respectively, and owing to the interception of downward long-wave radiation from dust layer aloft, radiative cooling was weakened above ground in the NCP.

3.3. Effects on PBL meteorology

3.3.1. Surface response

The energy re-allocation caused by dust radiative effect then leads to the subsequent adjustments in meteorological conditions, particularly in the planet boundary layer with fast hydrological cycle and energy exchange (Huang et al., 2014). In Fig. 6, surface temperature and relative humidity simulated by CTL and RFB were compared in terms of time series and 4-day averaged diurnal variation. Influenced by dust-radiation interaction, temperature at Beijing decreased in daytime and increased at night, with a maximum difference up to −1.5 °C and 2 °C during the episode. Take a site in dust source region for instance, at Minqin, temperature responded mainly in daytime with a largest cooling effects of −2 °C. The weak surface heating at night was associated with offset of energy deficit during daytime. Changes of relative humidity were almost opposite of temperature, with an overall increase at these two sites, which may facilitate aerosol hydroscopic growth and then aggravate pollution (Howell et al., 2006). Significantly, simulation of surface temperature and relative humidity with dust radiative feedbacks was closer to observation than without, which suggested an improvement of prediction accuracy by including dust aerosol radiative feedbacks during dust storm episodes.

On 6 April, a strong dust storm took place and transported

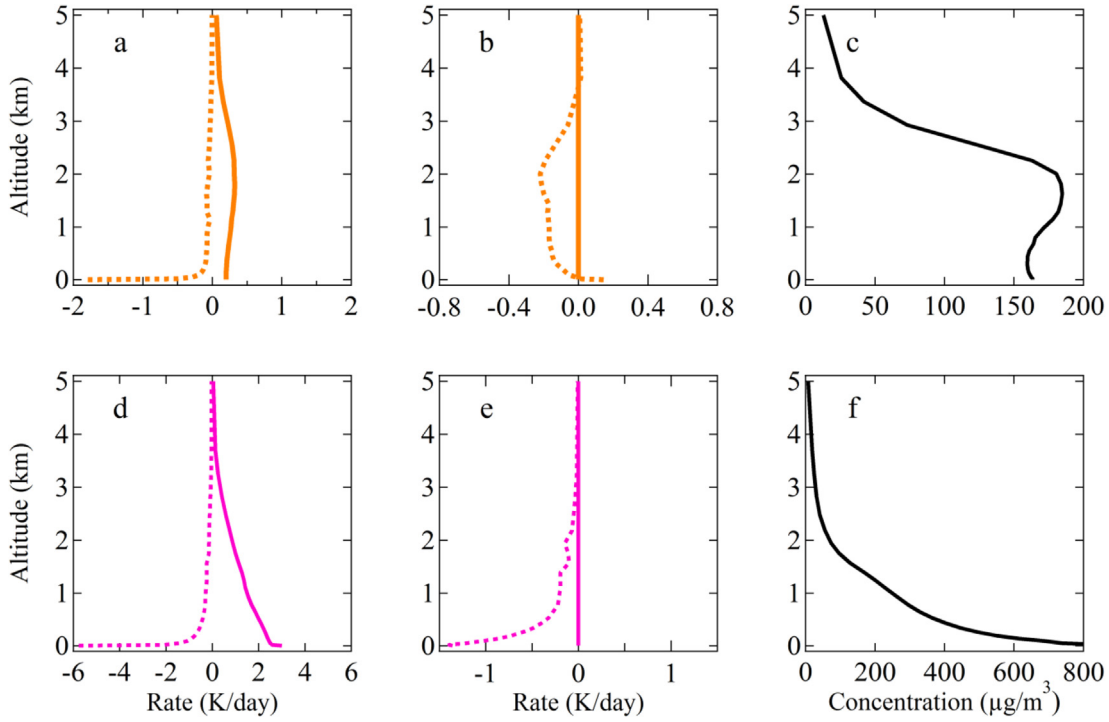

Fig. 5. Heating rates averaged over daytime (a, d), nighttime (b, e), and daily mean dust concentration profile (c, f) during 5–8 April, 2011, in the NCP (top panel) and the source region (bottom panel), respectively. Solid and dashed lines represent short-wave and long-wave radiation effects, respectively.

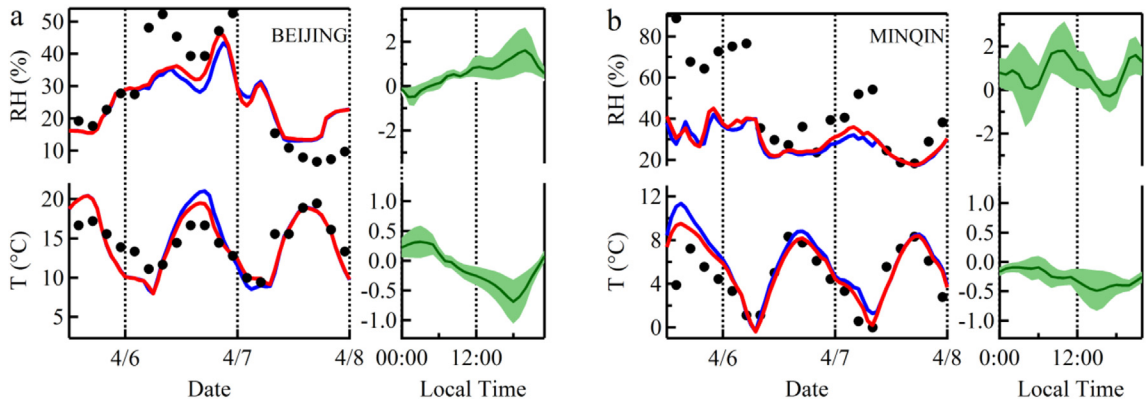

Fig. 6. Time evolution of surface temperature and relative humidity from CTL (blue lines), RFB (red lines) and corresponding observations (black dots) at Beijing and Minqin during 5–8 April, 2011. The green lines and shaded areas denote the diurnal variation and standard deviation of the difference between RFB and CTL averaged during the time span. (For interpretation of the references to colour in this figure legend, the reader is referred to the web version of this article.)

rapidly to the NCP (Fig. 3). The surface temperature response averaged during daytime and nighttime for this event are illustrated in Fig. 7. At daytime air temperature shows a general reduction, with the largest surface cooling exceeding −3 °C. The magnitude was slightly lower than the results given by Han et al. (2013), which was possibly due to the difference in storm strength as the AOD also showed a lower value in our case. It was noteworthy that a larger surface temperature decrease was found at downwind area compared with that at the source region, even with almost same abundance of dust. That was expected because windblown dust hitting the downwind area still suspended aloft after long-range transportation, and the influence of dust would be stronger at higher altitude with less absorbed heat transferred downward to the surface (Chung and Zhang, 2004; Zhu et al., 2007; Alizadeh Choobari et al., 2014). Contrary to the prevailing cooling effects during daytime, nocturnal surface temperature was increased by up to 2 °C, especially at rim area with little influence of energy loss in the daytime (Fig. 7b,d). Over the region where dust substantially affected during the daytime, however, temperature tended to decrease because of the relatively stronger negative net RF in the daytime than the positive effect at night.

3.3.2. PBL structure response

Fig. 8 compares observed temperature and relative humidity profile at 20:00 LT with two simulations (CTL and RFB). Temperature anomaly between RFB and CTL in the atmosphere (warming) and near the surface (cooling) was controversial, which exactly corresponded to the aforementioned heating pattern. In Chifeng, Minqin and Yuzhong, the warming adjustment occurred evidently at the altitude where the temperature lapse rate changed so as to be

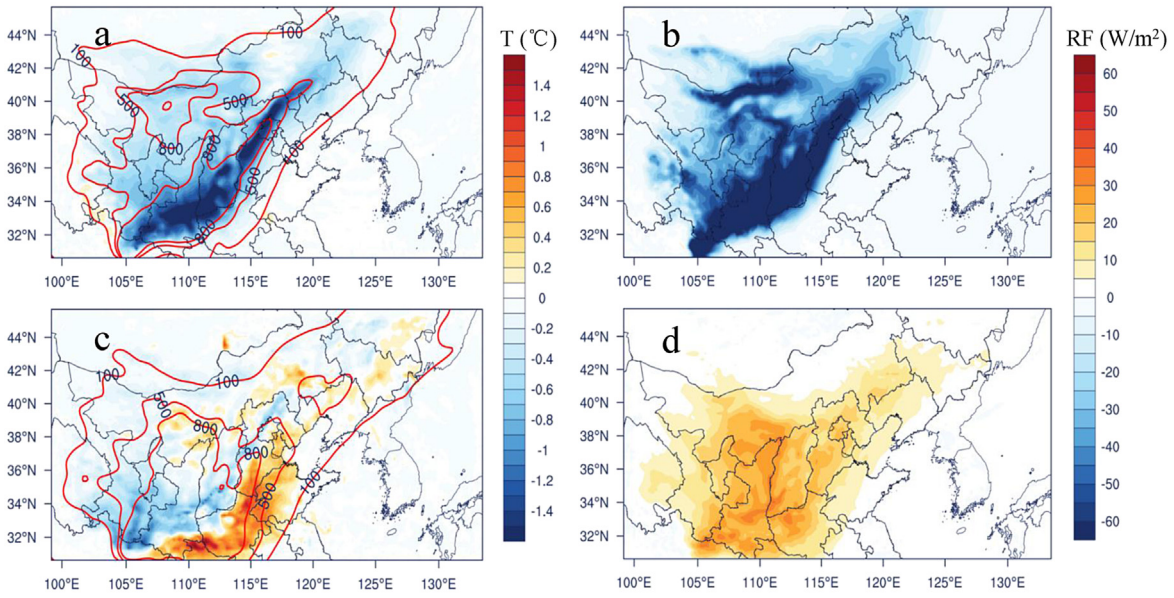

Fig. 7. Spatial distribution of surface temperature difference between RFB and CTL averaged for daytime (a) and nighttime (c) on 6 April, and the net RF at surface (b, d). The red lines represent column-integrated dust concentration (Unit: mg m^{-2}). (For interpretation of the references to colour in this figure legend, the reader is referred to the web version of this article.)

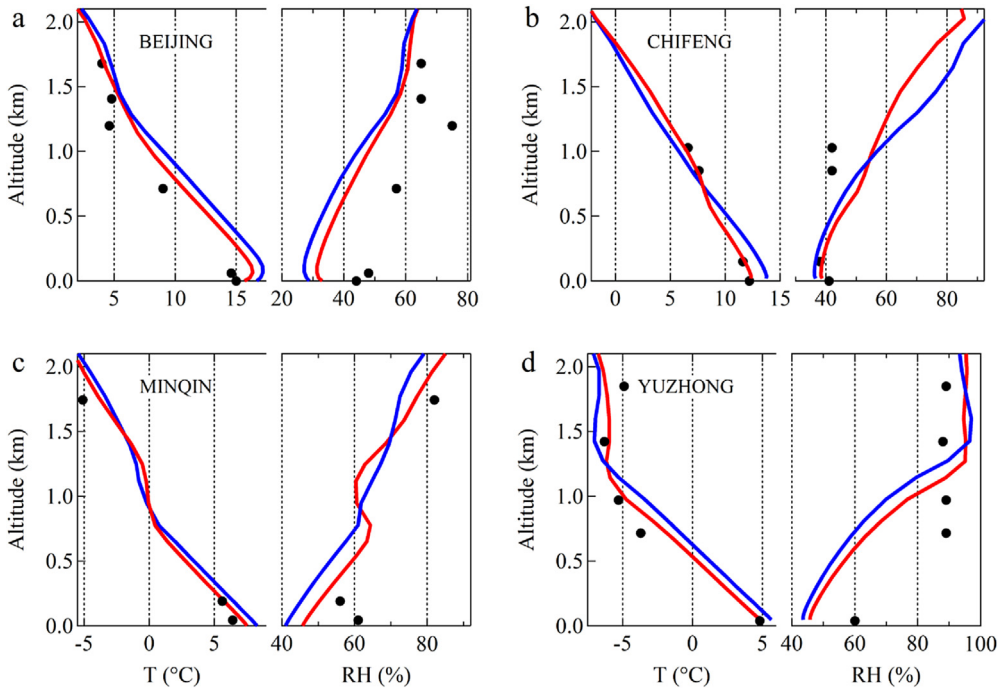

Fig. 8. Profiles of air temperature and relative humidity from CTL (blue lines), RFB (red lines) simulation and the corresponding radiosonde observations (black dots) at 20LT for 4 sites (Beijing on 6 April, Chifeng on 6 April, Minqin on 5 April, Yuzhong on 5 April). (For interpretation of the references to colour in this figure legend, the reader is referred to the web version of this article.)

recognized as the PBLH (Seidel et al., 2010). Note that the dust-induced warming near the top of PBL also existed in Beijing in daytime (not shown), although ended before the sounding time due to the deposition of dust aerosols from high altitude downward to the surface. The warming and cooling effects narrowed the bias between observation and CTL simulation with a maximum of more than 1 °C. The vertical distribution of response in air temperature and wind speed exhibited significant diurnal variation, as shown in Fig. 9. Lower surface temperature along with the solar heating of dust layer increased daytime atmospheric stability, and then reduced the downward transfer of momentum flux, which led to an averaged moderation of −0.4 m s^{-1} (Table 3) in wind speed near the ground. Inversely at night, dust particles warmed the surface by trapping more outgoing infrared radiation, and simultaneously radiatively cooled the dust-laden air above ground. As a result, enhanced instability increased vertical transport of fast wind aloft

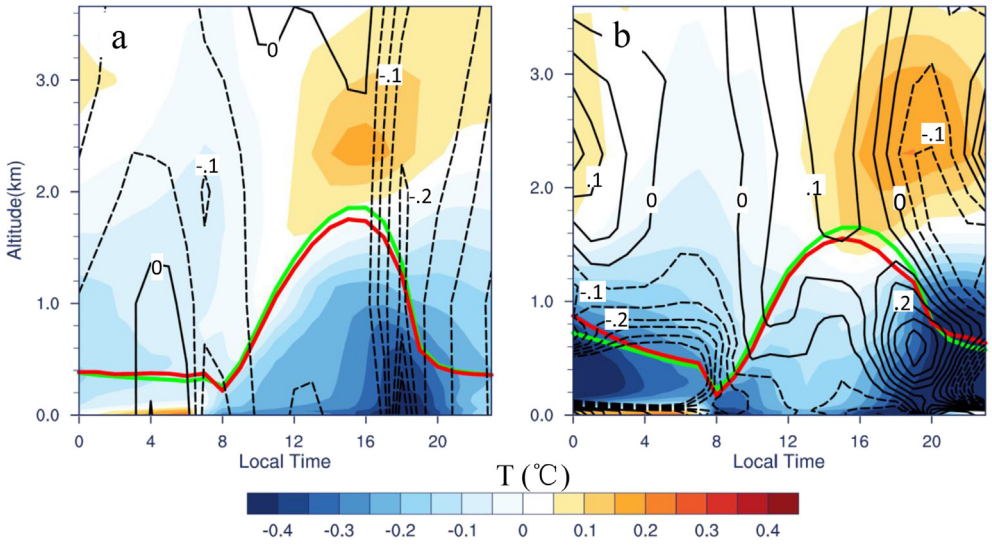

Fig. 9. Height-time cross-section of difference in air temperature (shaded color) and wind speed (black line, solid for positive value while dashed for negative) in the NCP (a) and the source region (b) averaged during 5–8 April. The red and green lines denote the PBL heights diagnosed by RFB and CTL, respectively.

to surface, by which surface wind was strengthened by up to 0.2 m s^{-1} (Table 3) at the source region.

PBLH is an important parameter which controls the turbulent mixing extent and governs the PBL-free troposphere exchange. In the YSU PBL scheme, PBLH on land is defined as the first height where a critical Richardson number calculated starting from surface (Ri_{cr}) exceeds 0.25, which indicates a strong reliance on heat exchange at air-surface interface and stratification in PBL (Hong, 2010). As shown in Fig. 9, the PBLH was depressed in daytime as the dust-induced atmospheric heating lowered the height of capping inversion (Fig. 8), and the averaged decrease at source area and at NCP was −90.2 m (Table 3) and −83.6 m respectively. At night, radiatively cooling by absorbing aerosols could move nocturnal elevated inversion upward (Bergstrom and Viskanta, 1973). In our case, the nocturnal PBLH rose up with a maximum of over 100 m at the source area.

3.4. *Effects on dust emission and long-range transport*

Considering the dependence of soil-derived dust deflation and deposition on meteorological fields, dust-induced responses in PBL would inevitably affect dust emission and the following transport process. Fig. 10 shows daily averaged changes of dust emission and column-integrated concentration caused by dust radiative feedbacks. Due to the reduction of surface wind speed, dust emission dropped down about 11.7 mg m^{-2} dy^{-1} during daytime. On contrast, nocturnal dust emission was strengthened by 0.2 mg m^{-2} dy^{-1}. Accordingly, averaged column dust loading at the source area dropped down by 17.1 mg m^{-2}. This decline was particularly remarkable during nighttime (−8.0 mg m^{-2} at day, −26.2 mg m^{-2} at night), which was consistent with previous estimates of a case study (Han et al., 2013). However, dust column concentration was intensified extensively over downwind area, which wasn't observed by multi-year simulation due to an offset by long-term average (Zhang et al., 2009). This effect was important for the downstream area, as it would cause deterioration in local air quality and enlarge the regional scope of dust storm.

Fig. 11 provides detailed view illustrating how the column-integrated dust content distributed vertically. Daily mean dust concentration difference during 5–8 April showed "increase-decrease-increase" pattern in both regions, with the negative response at around PBL top. The dust partitioning above and below PBL was about 4.5% and 2.4% at source region and 4.3% and 4.2% over the NCP. The cross-section of dust extinction coefficient at 532 nm along CALIPSO satellite track on 18:03 UTC 8 April (Fig. 12) depicted the transport pathway of mineral dust from higher altitude in western China to downwind area. Relative to CTL, RFB exhibited heavier load of dust aerosol, especially at higher altitude

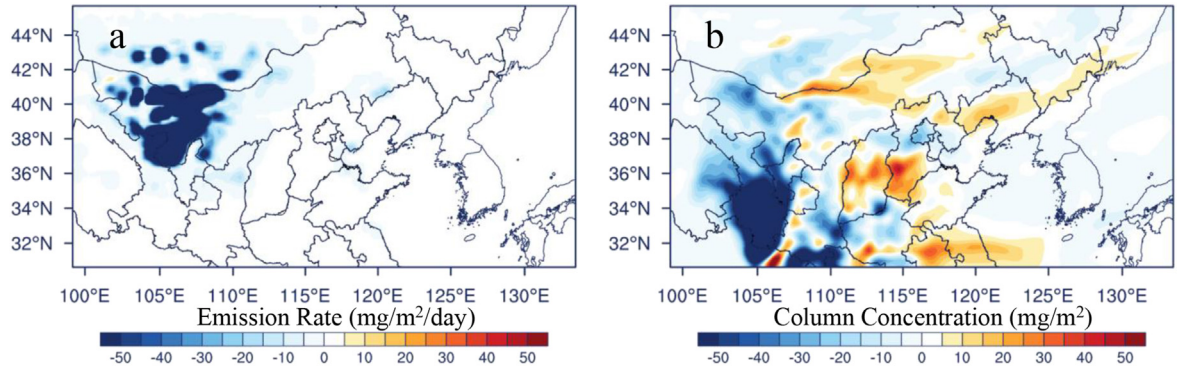

Fig. 10. Spatial distribution of daily averaged difference in dust emission (a) and column dust concentration (b) between RFB and CTL during 5–8 April.

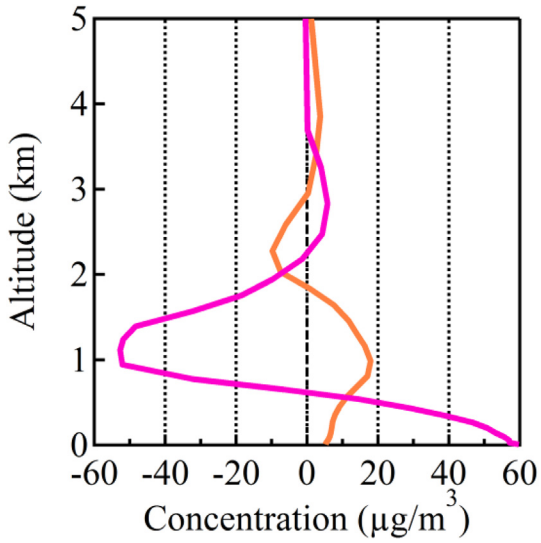

Fig. 11. Vertical profiles of daily averaged difference in dust concentration between RFB and CTL in the NCP (orange) and the source region (magenta) during 5–8 April. (For interpretation of the references to colour in this figure legend, the reader is referred to the web version of this article.)

meteorology and the emission and transport of dust. Due to the scattering and absorbing of solar and infrared radiation, dust aerosol exerted notable perturbations on earth-atmosphere energy budgets. The estimated daily mean short-wave RF over the source area was −34.6 W m^{-2} at the surface and 24.6 W m^{-2} in the atmosphere, while the long-wave RF was 13.5 W m^{-2} at the surface and −11.9 W m^{-2} in the atmosphere, indicating a counteracting effect of the two wavelength spectrum. In the daytime, the negative short-wave surface RF was dominant and resulted in a net energy loss, which was partially balanced by sensitive and latent heat flux. The net effect of the long-wave cooling and short-wave heating caused an air-temperature decrease near the ground surface while an increase in the upper air. The modification of temperature profile stabilized PBL and lowered the PBLH. In the nighttime, with the absence of short-wave radiation, long-wave RF of dust yielded opposite responses. The magnitude of response at night was comparative to that during daytime, implying that long-wave radiative effect played a non-negligible role in the dust radiative effect.

Dust radiative effects showed distinguishable characteristics between the source region and the downwind NCP, since dust RF was sensitive to dust loading, vertical distribution, and also surface albedo. Averaged over the whole episode, surface short-wave and

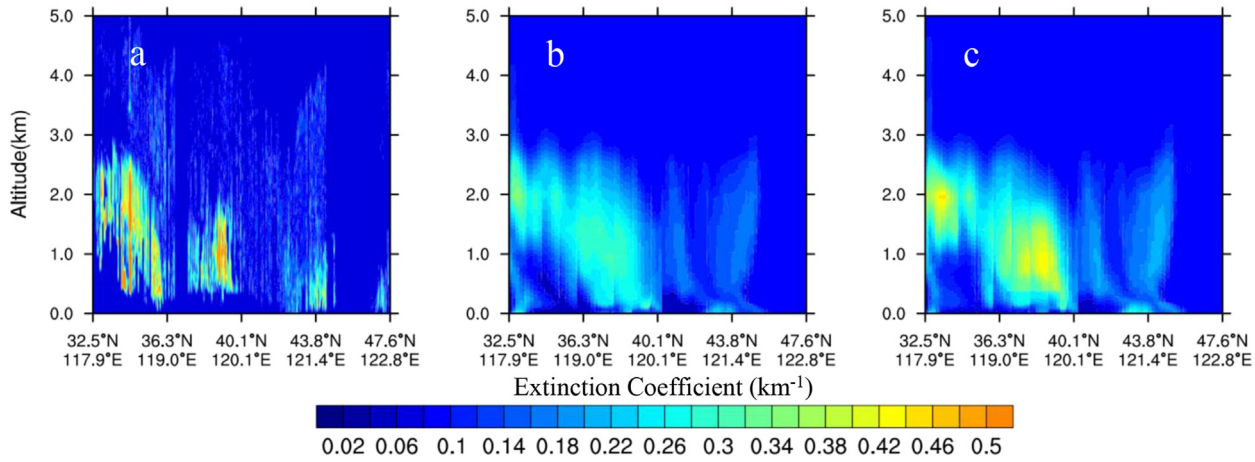

Fig. 12. Vertical cross-section of dust extinction coefficient at 532 nm along the CALIPSO satellite track by observation (a) and model simulation without (b) and with (c) feedback on 18:03 UTC 8 April 2011.

above 1 km, which was more close to satellite observation. It was speculated that the enhanced PBLH along with the dust emission at night (as discussed before) lifted more dust aerosols to upper PBL, where aerosols could be transported further, thus had longer residence time in the atmosphere (Bolin et al., 1974). In daytime, although the weakened wind speed confined dust emission, the decreased PBLH depressed dust within the PBL to a shallower layer, which was responsible for the increase of dust aerosols at lower boundary layer. In turn, the increased dust loading, especially the concentration peak above PBL top would further amplify the RF, triggering a feedback loop between dust concentration and PBL meteorology at downwind region.

4. Conclusions

Based on a typical Asian dust episode during 5–8 April, 2011, we used a fully coupled meteorology-chemistry model WRF-Chem to simulate the impacts of dust-radiation interaction on PBL long-wave RF at the NCP were smaller than at the source region due to less dust abundance, but the instantaneous surface temperature response at the NCP could be greater when dust storm reached from a higher altitude. Great surface energy deficit during the day offset largely the enhanced energy margin associated with increased downward terrestrial radiation at night, leading to a weak warming effect at the source region.

When coupling back to the dust emission and transport, a mean decrease of 17.1 mg m^{-2} (average of daytime and nighttime) in dust loading caused by less dust emissions associated with moderated surface wind was found at the source region. Nevertheless, dust loading in the NCP increased by 5.4 mg m^{-2}. Stabilized PBL stratification suppressed dust aerosols within a lower PBL, which added with nocturnal intensified emission and was transported higher across PBL top by enhanced PBLH at night. With little friction and turbulent mixing, windblown dust was transported further in free atmosphere, thereby prolonging its lifetime. Therefore, long-wave radiation effects worked more than to offset, but to cooperate

with the contrast effects by short-wave radiation.

Evaluated against observation, model simulation with dust-radiation interaction showed superiority over that without such feedbacks in terms of not only the surface meteorological element but also the vertical atmospheric profiles, which indicated the necessity to include dust-radiation coupling in numerical weather prediction. In this study, we only considered aerosol-radiation interaction. As an important kind of cloud condensation nuclei (CCN), dust aerosols remarkably affect cloud such as cloud microphysical property, cloud fraction and cloud lifetime (Huang et al., 2014), which is critical in numerical weather simulation. Dust-cloud interactions will be included in future works to give a thorough assessment of dust-meteorology feedback.

Acknowledgments

This work was supported by Natural Science Foundation of China (D0512/41422504, D0510/41505109, and D0512/91544231) and National Key Technology Research and Development Program (2014BAC22B04). Part of this work was supported by the Jiangsu Provincial Science Fund for Distinguished Young Scholars awarded to A.J. Ding (No. BK20140021). We thank the principal investigator of AERONET sites for the availability of AERONET data. The observation data are provided by NOAA's National Climatic Data Center.

References

Ahn, H.J., Park, S.U., Chang, L.S., 2007. Effect of direct radiative forcing of Asian dust on the meteorological fields in east Asia during an Asian dust event period. J. Appl. Meteorol. Climatol. 46, 1655–1681.
Alizadeh Choobari, O., Zawar-Reza, P., Sturman, A., 2012. Feedback between wind-blown dust and planetary boundary-layer characteristics: sensitivity to boundary and surface layer parameterizations. Atmos. Environ. 61, 294–304.
Alizadeh Choobari, O., Zawar-Reza, P., Sturman, A., 2014. The global distribution of mineral dust and its impacts on the climate system: a review. Atmos. Res. 138, 152–165.
Alpert, P., Kaufman, Y.J., Shay-El, Y., Tanre, D., da Silva, A., Schubert, S., Joseph, J.H., 1998. Quantification of dust-forced heating of the lower troposphere. Nature 395, 367–370.
Bergstrom, R.W., Viskanta, R., 1973. Modeling of the effects of gaseous and particulate pollutants in the Urban atmosphere. Part I: thermal structure. J. Appl. Meteorol. 12, 901–912.
Bolin, B., Aspling, G., Persson, C., 1974. Residence time of atmospheric pollutants as dependent on source characteristics, atmospheric diffusion processes and sink mechanisms. Tellus 26, 185–195.
Brindley, H.E., Russell, J.E., 2009. An assessment of Saharan dust loading and the corresponding cloud-free longwave direct radiative effect from geostationary satellite observations. J. Geophys. Res. 114, D23201.
Chen, S., Huang, J., Zhao, C., Qian, Y., Leung, L.R., Yang, B., 2013. Modeling the transport and radiative forcing of Taklimakan dust over the Tibetan plateau: a case study in the summer of 2006. J. Geophys. Res. 118, 797–812.
Chun, Y., Boo, K.O., Kim, J., Park, S.U., Lee, M., 2001. Synopsis, transport, and physical characteristics of Asian dust in Korea. J. Geophys. Res. 106, 18461–18469.
Chung, C.E., Zhang, G.J., 2004. Impact of absorbing aerosol on precipitation: dynamic aspects in association with convective available potential energy and convective parameterization closure and dependence on aerosol heating profile. J. Geophys. Res. 109, D22103.
Costa, M.J., Sohn, B.J., Levizzani, V., Silva, A.M., 2006. Radiative forcing of Asian dust determined from the synergized GOME and GMS satellite data - a case study. J. Meteorol. Soc. Jpn. 84, 85–95.
Dey, S., 2004. Influence of dust storms on the aerosol optical properties over the Indo-Gangetic basin. J. Geophys. Res. 109, D20211.
Ding, A.J., Fu, C.B., Yang, X.Q., Sun, J.N., Petäjä, T., Kerminen, V.M., Wang, T., Xie, Y., Herrmann, E., Zheng, L.F., Nie, W., Liu, Q., Wei, X.L., Kulmala, M., 2013. Intense atmospheric pollution modifies weather: a case of mixed biomass burning with fossil fuel combustion pollution in eastern China. Atmos. Chem. Phys. 13 (20), 10545–10554.
Fast, J.D., Gustafson, W.I., Easter, R.C., Zaveri, R.A., Barnard, J.C., Chapman, E.G., Grell, G.A., Peckham, S.E., 2006. Evolution of ozone, particulates, and aerosol direct radiative forcing in the vicinity of Houston using a fully coupled meteorology-chemistry-aerosol model. J. Geophys. Res. 111, D21305.
Forkel, R., Werhahn, J., Hansen, A.B., McKeen, S., Peckham, S., Grell, G., Suppan, P., 2012. Effect of aerosol-radiation feedback on regional air quality – a case study with WRF/Chem. Atmos. Environ. 53, 202–211.
Fukushima, H., Toratani, M., Yamamiya, S., Mitomi, Y., 2000. Atmospheric correction algorithms for ADEOS/OCTS ocean color data: performance comparison based on Ship and Buoy measurements. Adv. Space Res. 25, 1015–1024.
Ge, J.M., Su, J., Ackerman, T.P., Fu, Q., Huang, J.P., Shi, J.S., 2010. Dust aerosol optical properties retrieval and radiative forcing over northwestern China during the 2008 China-U.S. joint field experiment. J. Geophys. Res. 115, D00K12.
Ginoux, P., Chin, M., Tegen, I., Prospero, J.M., Holben, B., Dubovik, O., Lin, S.-J., 2001. Sources and distributions of dust aerosols simulated with the GOCART model. J. Geophys. Res. 106, 20255–20273.
Grell, G.A., Peckham, S.E., Schmitz, R., McKeen, S.A., Frost, G., Skamarock, W.C., Eder, B., 2005. Fully coupled "online" chemistry within the WRF model. Atmos. Environ. 39 (37), 6957–6975.
Han, Z., Li, J., Guo, W., Xiong, Z., Zhang, W., 2013. A study of dust radiative feedback on dust cycle and meteorology over East Asia by a coupled regional climate-chemistry-aerosol model. Atmos. Environ. 68, 54–63.
Han, Z., Li, J., Xia, X., Zhang, R., 2012. Investigation of direct radiative effects of aerosols in dust storm season over East Asia with an online coupled regional climate-chemistry-aerosol model. Atmos. Environ. 54, 688–699.
Hess, M., Koepke, P., Schult, I., 1998. Optical properties of aerosols and clouds: the software package OPAC. B Am. Meteorol. Soc. 79, 831–844.
Holben, B.N., Tanré, D., Smirnov, A., Eck, T.F., Slutsker, I., Abuhassan, N., Newcomb, W.W., Schafer, J.S., Chatenet, B., Lavenu, F., Kaufman, Y.J., Castle, J.V., Setzer, A., Markham, B., Clark, D., Frouin, R., Halthore, R., Karneli, A., O'Neill, N.T., Pietras, C., Pinker, R.T., Voss, K., Zibordi, G., 2001. An emerging ground-based aerosol climatology: aerosol optical depth from AERONET. J. Geophys. Res. 106, 12067–12097.
Hong, S.Y., 2010. A new stable boundary-layer mixing scheme and its impact on the simulated East Asian summer monsoon. Q. J. R. Meteorol. Soc. 136, 1481–1496.
Howell, S.G., Clarke, A.D., Shinozuka, Y., Kapustin, V., McNaughton, C.S., Huebert, B.J., Doherty, S.J., Anderson, T.L., 2006. Influence of relative humidity upon pollution and dust during ACE-Asia: size distributions and implications for optical properties. J. Geophys. Res. 111, D06205.
Huang, J., Fu, Q., Su, J., Tang, Q., Minnis, P., Hu, Y., Yi, Y., Zhao, Q., 2009. Taklimakan dust aerosol radiative heating derived from CALIPSO observations using the Fu-Liou radiation model with CERES constraints. Atmos. Chem. Phys. 9 (12), 4011–4021.
Huang, J.P., Lin, B., Minnis, P., Wang, T.H., Wang, X., Hu, Y.X., Yi, Y.H., Ayers, J.K., 2006. Satellite-based assessment of possible dust aerosols semi-direct effect on cloud water path over East Asia. Geophys. Res. Lett. 33.
Huang, J.P., Wang, T.H., Wang, W.C., Li, Z.Q., Yan, H.R., 2014. Climate effects of dust aerosols over East Asian arid and semiarid regions. J. Geophys. Res. 119, 11398–11416.
Huang, X., Song, Y., Zhao, C., Cai, X.H., Zhang, H.S., Zhu, T., 2015. Direct radiative effect by multicomponent aerosol over China. J. Clim. 28, 3472–3495.
Husar, R.B., Tratt, D.M., Schichtel, B.A., Falke, S.R., Li, F., Jaffe, D., Gassó, S., Gill, T., Laulainen, N.S., Lu, F., Reheis, M.C., Chun, Y., Westphal, D., Holben, B.N., Gueymard, C., McKendry, I., Kuring, N., Feldman, G.C., McClain, C., Frouin, R.J., Merrill, J., DuBois, D., Vignola, F., Murayama, T., Nickovic, S., Wilson, W.E., Sassen, K., Sugimoto, N., Malm, W.C., 2001. Asian dust events of April 1998. J. Geophys. Res. 106, 18317–18330.
In, H.J., Park, S.U., 2002. A simulation of long-range transport of yellow sand observed in April 1998 in Korea. Atmos. Environ. 36 (26), 4173–4187.
IPCC, 2013. Intergovernmental Panel on Climate Change (IPCC) Fifth Assessment Report: Climate Change 2013 (AR5).
Kuhlmann, J., Quaas, J., 2010. How can aerosols affect the Asian summer monsoon? Assessment during three consecutive pre-monsoon seasons from CALIPSO satellite data. Atmos. Chem. Phys. 10 (10), 4673–4688.
Liu, Y., Huang, J., Shi, G., Takamura, T., Khatri, P., Bi, J., Shi, J., Wang, T., Wang, X., Zhang, B., 2011. Aerosol optical properties and radiative effect determined from sky-radiometer over Loess plateau of Northwest China. Atmos. Chem. Phys. 11 (22), 11455–11463.
Liu, Z.Y., Fairlie, T.D., Uno, I., Huang, J.F., Wu, D., Omar, A., Kar, J., Vaughan, M., Rogers, R., Winker, D., Trepte, C., Hu, Y.X., Sun, W.B., Lin, B., Cheng, A.N., 2013. Transpacific transport and evolution of the optical properties of Asian dust. J. Quant. Spectrosc. Radiat. Transf. 116, 24–33.
Logan, T., Xi, B.K., Dong, X.Q., 2013. A comparison of the Mineral dust absorptive properties between two Asian dust events. Atmos. Basel. 4, 1–16.
Miller, R.L., 2004. Surface radiative forcing by soil dust aerosols and the hydrologic cycle. J. Geophys. Res. 109, D04203.
Nakajima, T., Tanaka, M., Yamano, M., Shiobara, M., Arao, K., Nakanishi, Y., 1989. Aerosol optical characteristics in the Yellow Sand Events observed in May, 1982 at Nagasaki .2. Models. J. Meteorol. Soc. Jpn. 67, 279–291.
Nie, W., Ding, A.J., Wang, T., Kerminen, V.M., George, C., Xue, L.K., Wang, W.X., Zhang, Q.Z., Petaja, T., Qi, X.M., Gao, X.M., Wang, X.F., Yang, X.Q., Fu, C.B., Kulmala, M., 2014. Polluted dust promotes new particle formation and growth. Sci. Rep. 4.
Park, S., Chang, L., Lee, E., 2005. Direct radiative forcing due to aerosols in East Asia during a Hwangsa (Asian dust) event observed on 19-23 March 2002 in Korea. Atmos. Environ. 39 (14), 2593–2606.
Seidel, D.J., Ao, C.O., Li, K., 2010. Estimating climatological planetary boundary layer heights from radiosonde observations: comparison of methods and uncertainty analysis. J. Geophys. Res. 115, D16113.
Seinfeld, J.H., Carmichael, G.R., Arimoto, R., Conant, W.C., Brechtel, F.J., Bates, T.S., Cahill, T.A., Clarke, A.D., Doherty, S.J., Flatau, P.J., Huebert, B.J., Kim, J., Markowicz, K.M., Quinn, P.K., Russell, L.M., Russell, P.B., Shimizu, A., Shinozuka, Y., Song, C.H., Tang, Y., Uno, I., Vogelmann, A.M., Weber, R.J., Woo, J.-H., Zhang, X.Y., 2004. ACE-ASIA: regional climatic and atmospheric chemical

effects of asian dust and pollution. Bull. Am. Meteorol. Soc. 85, 367–380.
Stier, P., Seinfeld, J.H., Kinne, S., Boucher, O., 2007. Aerosol absorption and radiative forcing. Atmos. Chem. Phys. 7 (19), 5237–5261.
Stone, R.S., Anderson, G.P., Andrews, E., Dutton, E.G., Shettle, E.P., 2007. Incursions and radiative impact of Asian dust in northern Alaska. Geophys. Res. Lett. 34.
Tegen, I., Schepanski, K., 2009. The global distribution of mineral dust. IOP Conf. Ser. 7, 012001.
Wang, H., Shi, G., Zhu, J., Chen, B., Che, H., Zhao, T., 2013. Case study of longwave contribution to dust radiative effects over East Asia. Chin. Sci. Bull. 58, 3673–3681.
Wang, J., Wang, S., Jiang, J., Ding, A., Zheng, M., Zhao, B., Wong, D.C., Zhou, W., Zheng, G., Wang, L., Pleim, J.E., Hao, J., 2014. Impact of aerosol–meteorology interactions on fine particle pollution during China's severe haze episode in January 2013. Environ. Res. Let. 9, 94002–94008.
Wang, W., Cheng, T., Zhang, R., Jia, X., Han, Z., Zhang, X., Xu, X., Li, D., 2010. Insights into an Asian dust event sweeping Beijing during April 2006: particle chemical composition, boundary layer structure, and radiative forcing. J. Geophys. Res. 115, D18208.
Wu, Z.J., Cheng, Y.F., Hu, M., Wehner, B., Sugimoto, N., Wiedensohler, A., 2009. Dust events in Beijing, China (2004–2006): comparison of ground-based measurements with columnar integrated observations. Atmos. Chem. Phys. 9 (18), 6915–6932.
Xie, Y., Ding, A., Nie, W., Mao, H., Qi, X., Huang, X., Xu, Z., Kerminen, V.M., Petäjä, T., Chi, X., 2015. Enhanced sulfate formation by nitrogen dioxide: implications from in-situ observations at the SORPES Station. J. Geophys. Res. Atmos. 120 http://dx.doi.org/10.1002/2015JD023607.
Yuan, H., Zhuang, G., Li, J., Wang, Z., Li, J., 2008. Mixing of mineral with pollution aerosols in dust season in Beijing: revealed by source apportionment study. Atmos. Environ. 42 (9), 2141–2157.
Yue, X., Wang, H., Liao, H., Fan, K., 2010. Simulation of dust aerosol radiative feedback using the GMOD: 2. Dust-climate interactions. J. Geophys. Res. 115, D04201.
Zaveri, R.A., Easter, R.C., Fast, J.D., Peters, L.K., 2008. Model for simulating aerosol interactions and chemistry (MOSAIC). J. Geophys. Res. 113, D13204.
Zaveri, R.A., Peters, L.K., 1999. A new lumped structure photochemical mechanism for large-scale applications. J. Geophys. Res. 104, 30387–30415.
Zhang, D.F., Zakey, A.S., Gao, X.J., Giorgi, F., Solmon, F., 2009. Simulation of dust aerosol and its regional feedbacks over East Asia using a regional climate model. Atmos. Chem. Phys. 9 (4), 1095–1110.
Zhang, R., 2005. Ground observations of a strong dust storm in Beijing in March 2002. J. Geophys. Res. 110, D18S06.
Zhang, X.Y., 2003. Characterization of soil dust aerosol in China and its transport and distribution during 2001 ACE-Asia: 1. Network observations. J. Geophys. Res. 108 (D9).
Zhang, X.Y., Arimoto, R., An, Z.S., 1997. Dust emission from Chinese desert sources linked to variations in atmospheric circulation. J. Geophys. Res. 102, 28041–28047.
Zhao, C., Liu, X., Leung, L.R., Johnson, B., McFarlane, S.A., Gustafson, W.I., Fast, J.D., Easter, R., 2010. The spatial distribution of mineral dust and its shortwave radiative forcing over North Africa: modeling sensitivities to dust emissions and aerosol size treatments. Atmos. Chem. Phys. 10, 8821–8838.
Zhao, C., Liu, X., Ruby Leung, L., Hagos, S., 2011. Radiative impact of mineral dust on monsoon precipitation variability over West Africa. Atmos. Chem. Phys. 11 (5), 1879–1893.
Zhu, A., Ramanathan, V., Li, F., Kim, D., 2007. Dust plumes over the Pacific, Indian, and Atlantic oceans: climatology and radiative impact. J. Geophys. Res. 112, D16208.